Icarus 269 (2016) 91–97

Contents lists available at ScienceDirect

Icarus

journal homepage: www.elsevier.com/locate/icarus

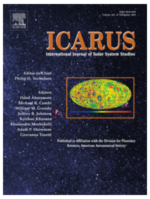

Emission of energetic neutral atoms from water ice under Ganymede surface-like conditions

Martin Wieser[a,*], Yoshifumi Futaana[a], Stas Barabash[a], Peter Wurz[b]

[a] Swedish Institute of Space Physics, Box 812, SE-98128 Kiruna, Sweden
[b] Physikalisches Institut, University of Bern, Sidlerstrasse 5, CH-3012 Bern, Switzerland

ARTICLE INFO

Article history:
Received 9 April 2015
Revised 27 November 2015
Accepted 19 December 2015
Available online 14 January 2016

Keywords:
Ganymede
Ice
Satellites, surfaces
Jupiter, satellites

ABSTRACT

The co-rotating plasma around Jupiter precipitates on the surfaces of the jovian moons, where it is not hindered by a local magnetic field. Precipitating ions lead to the emission of energetic neutral atoms, which are produced via backscattering and sputtering processes, from the surface. The European Space Agency's JUICE mission to Jupiter carries as part of the Particle Environment Package experiment an imaging energetic neutral atom spectrometer called the jovian Neutrals Analyzer (JNA). When it is in orbit around Ganymede, JNA will measure the energetic neutral atom flux emitted from the surface of Ganymede in the energy range from 10 eV to 3300 eV. The surface of Ganymede consists of a large fraction of water ice. To characterize the expected energetic neutral atom fluxes from water ice due to precipitating jovian plasma, we impacted protons and singly charged oxygen ions with energies up to 33 keV on a salty water ice target kept at Ganymede surface conditions. Emitted energetic atoms were measured energy- and mass-resolved using the JNA prototype instrument. The data show high yields for energetic neutral atoms per incident ion in the JNA energy range. For incident protons, energetic neutral atom yields between 0.28 at 1 keV and ~40 at 33 keV were observed. For incident singly charged oxygen ions, the observed energetic neutral atom yield ranged from 0.8 for at 3 keV to ~170 at 23 keV.

1. Introduction

Jupiter possesses a large magnetosphere that extends far beyond the orbits of the Galilean moons. These moons are constantly exposed to the co-rotating flow of jovian magnetospheric plasma (Khurana, 1997). In the absence of an atmosphere and when it is not hindered by an intrinsic local magnetic field, this plasma reaches the surface and interacts directly with surface materials. The sputtering of surface materials by incident ions results in a flux of energetic neutral atoms (ENA) leaving the surface (Shi et al., 1995; Ip et al., 1997; Johnson, 1998; Cooper et al., 2001; Baragiola et al., 2003; Famá et al., 2008) that contribute to the formation of extended exospheres (Wurz et al., 2010). The energy distribution of these ENAs is dominated by energies below 10s of eV (Sigmund, 1969; Betz and Wien, 1994) and, in the context of planetary science, has a cutoff at approximately 100 eV (Wurz and Lammer, 2003; Wurz et al., 2007). A fraction of the impinging ion flux is expected to backscatter to space as ENAs, despite the large expected surface roughness. For comparison, from the regolith covered rocky surface of the Moon, up to 20% of the impinging solar wind protons are backscattered as hydrogen ENAs (Wieser et al., 2009). These backscattered ENAs have substantial energies far above those of the ENAs produced by electronic sputtering, with up to 50% of the impinging solar wind protons (Wieser et al., 2009; Futaana et al., 2012). It is expected that in the jovian system, a similarly large fraction of the impinging co-rotating plasma ions are backscattered from the icy moons' surfaces as ENAs. On Ganymede, the surface is partially shielded from the magnetospheric plasma inflow by Ganymede's intrinsic magnetic field (Cooper et al., 2001; Khurana et al., 2007). Imaging the ENA flux from the surface will make visible the boundaries of the regions, where plasma is able to reach the surface nevertheless, i.e., at the polar caps. This method is similar to how magnetic anomalies on the Moon were imaged (Wieser et al., 2010).

Experimental data for the emission of ENAs from ices as found, e.g., on Ganymede's surface (Showman and Malhotra, 1999) when it is bombarded with ions in the keV to 10s of keV energy range, usually focus on the total sputter yield; thus, little data exist regarding the energy spectra of the emitted ENAs (Shi et al., 1995; Ip et al., 1997; Johnson, 1998; Baragiola et al., 2003; Famá et al., 2008). This is due to the difficulty in measuring ENAs in the energy range from 10s of eV up to a few keV.

---

[*] Corresponding author.
E-mail address: wieser@irf.se (M. Wieser).

http://dx.doi.org/10.1016/j.icarus.2015.12.043
0019-1035/

We present mass resolved measurements of the emitted ENA energy spectrum from 10s of eV up to a few keV that were obtained from an icy surface bombarded with positive ions. We estimate energetic neutral atom yields for emitted ENAs with energies above 15 eV. The experiment was performed in the MEFISTO test facility at the University of Bern (Marti et al., 2001). A prototype model of the jovian Neutrals Analyzer (JNA) was used as the energy and mass resolving ENA detector. The JNA instrument is based on the Energetic Neutral Atom instrument (Kazama et al., 2007), which is part of the payload of the Mercury Magnetospheric Orbiter of the BepiColombo mission to Mercury. A similar instrument, the Chandrayaan Energetic Neutral Atom analyzer, was successfully flown on the Indian Chandrayaan-1 mission to the Moon (Barabash et al., 2009). JNA was selected to fly as part of the Particle Environment Package (PEP) (Barabash et al., 2013) on ESA's Jupiter Icy moons Explorer (JUICE) (Grasset et al., 2013). The science objectives of JNA are closely tied to the interaction of ions with ices. While it is in orbit around Ganymede, JNA will map the precipitation pattern of ions on the surface via sputtered and backscattered ENAs. JNA measurements will constrain the magnetic field topology on the surface of Ganymede, analogous to CENA measurements on the Moon (Wieser et al., 2010). JNA will also observe the dynamics of the Io plasma torus remotely via ENAs that are generated through charge exchange with the neutral gas background (Futaana et al., 2015).

2. Experimental setup

The experimental setup (Fig. 1) consisted of an ice disk exposed to an incident ion beam. Energetic neutral atoms emitted from the ice disk were measured using a prototype of the JNA instrument. The JNA prototype was mounted such that it measured energetic neutral atoms emitted at angles centered on the specular reflection direction from the ice disk. The pencil ion beam provided by the MEFISTO test facility was 5 mm in diameter and directed at a grazing incidence angle Φ of 83° to the surface normal to the ice disk (Fig. 1). Monoenergetic beams of H^+ and O^+ ions were used, with energies between 1 keV and 33 keV. The ion beam intensity was periodically measured with a Faraday cup. Typical ion beam currents were on the order of 1 nA.

The ice disk was prepared from a mixture of 11 g NaCl and 150 ml H_2O, frozen in a plastic dish placed on dry ice. The salt concentration corresponded to approximately twice the salt concentration found in typical terrestrial seawater. Ice from such a solution contains two distinct phases: H_2O (water ice) and $NaCl{\cdot}2H_2O$ (hydrohalite), with the water ice phase dominating (e.g., McCarthy et al., 2007). NaCl was added to simulate impurities in the ice block and to provide some electrical conductivity. The latter prevented the buildup of charges on the scattering surface during ion bombardment. The ice block was then roughly shaped using very coarsely grained glass sand paper to a flat disk of approximately 10 cm in diameter and a few mm in thickness. The surface roughness R_a after polishing was estimated to be 0.2 mm.

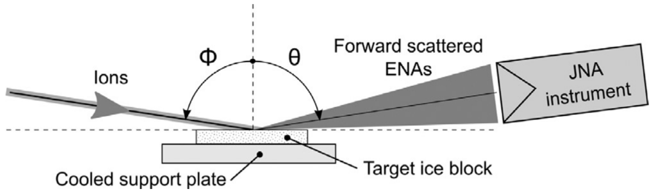

Fig. 1. Experiment geometry: an ion beam from the left hits the ice disk at a grazing incidence of $\Phi = 83°$ to the surface normal. The JNA prototype instrument records energetic neutral atoms emitted around the specular reflection direction $\theta = 83°$.

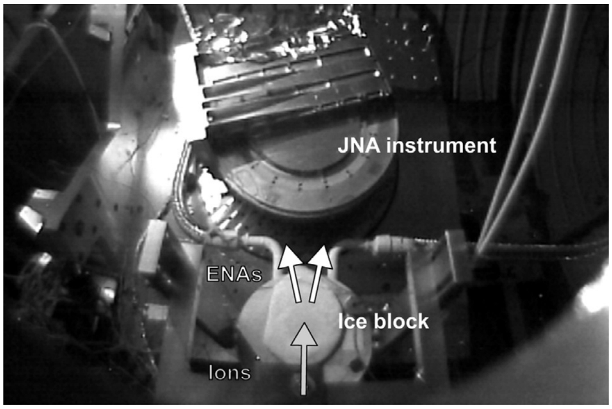

Fig. 2. View into vacuum system during the measurements, with ice block (bottom center) and JNA prototype instrument (top center). The ion beam hits the ice block from the lower edge of the image (lower arrow) and ENAs are scattered toward the JNA instrument (upper arrows). Below the ice disk, the cooled support with liquid nitrogen feeding lines is visible.

The resulting ice disk was white in color due to small-scale ice grain boundaries and additional frozen CO_2 bubbles originating from the dry ice. Fig. 2 shows the ice disk installed in the vacuum system. Vacuum conditions near the ice surface were determined by the vapor pressure of the ice. The conditions on the surface of Ganymede correspond well to a point on the vapor pressure curve for water at 10^{-7} mbar and a temperature of 150 K (−123 °C) (Murphy and Koop, 2005). A dedicated liquid nitrogen cooling system, keeping the temperature of the ice within a few degrees of 150 K, supported the ice disk. This temperature and the resulting vacuum pressure of approximately 10^{-7} mbar were maintained throughout the scattering experiment. At 150 K, the CO_2 enclosed in bubbles in the ice should freeze out. It is unlikely, however, that pure CO_2 ice was exposed to the ion beam. The vapor pressure of pure CO_2 ice at 150 K is approximately 13 mbar (James et al., 1992), and exposed CO_2 ice would have already sublimated quickly during the pump down process of the vacuum system. Indeed, CO_2 pressure spikes were observed during the early phases of the vacuum pump down process. However, a small amount of CO_2 was likely present in the ice as a mixed phase ice. CO_2 bound in surface ices was observed on Ganymede using infrared spectroscopy (McCord et al., 1997, 1998). However, we estimate that the exposed part of our ice disk contained less than 1 CO_2 molecule per 100 H_2O molecules, based on the monitored residual gas composition. A similar small amount of air may have been included in bubbles in the ice.

The JNA prototype measures energetic neutral atoms entering its aperture by reflecting them at grazing incidence on a charge conversion surface and thereby positively ionizing them. The newly generated positive ions are then energy analyzed and post-accelerated to keV energy and are finally detected in a time-of-flight section. Ions are prevented from entering the aperture by a charged particle deflection system. A detailed description of the ion optics can be found in Kazama et al. (2007). For this experiment, the JNA energy analyzer was programmed with 8 logarithmically spaced nominal center energies (20 eV, 40 eV, 80 eV, 160 eV, 320 eV, 640 eV, 1280 eV and 2560 eV). Combined with an energy resolution $\Delta E/E$ of approximately 100%, this resulted in dense coverage of an energy range from 15 eV to 3300 eV. Actual center energies are slightly species dependent due to the species dependent energy loss at the charge conversion surface of JNA. The angular resolution of the JNA prototype was 25° times 7° full width at half maximum; however, given the experimental setup used, the ENA emitting spot on the ice sample, as seen from JNA, was always much smaller than this and was completely contained within one angular pixel. The mass resolution of JNA allowed the separation of mass groups centered on $m = 1$ amu (“H”), 4 amu, 16 amu (“O-group”) and >32 amu (“heavy”). The O-group may also contain a H_2O component that cannot be distinguished from atomic oxygen due to a mass difference that is too small. In this paper, we generally use the term ‘oxygen group ENAs’ when referring to this oxygen/water mass group.

Calibration of ENA sensors at energies below 1 keV is a challenge, and the JNA instrument is no exception. For the measurements shown, we combined the instrument performance data obtained from flight units of the ENA sensors flown on Chandrayaan-1 and on BepiColombo. Both instruments are representative with respect to the performance of the JNA prototype used in this experiment. Energetic neutral beams of hydrogen and oxygen, produced by the MEFISTO system ion beam neutralizer (Wieser and Wurz, 2005), were used to confirm the sensitivity of the JNA prototype. The MEFISTO system is able to produce an energetic neutral hydrogen or oxygen beam in the energy range from 10 eV to 3 keV, with an energy width of approximately 15% for neutral hydrogen and approximately twice that value for neutral oxygen. This energy width is still small compared with the energy resolution of the JNA sensor.

3. Results

A total of 6 different ENA production channels were investigated: H^+ and O^+ incident ions producing H, O and ‘heavy’ ENAs, with ‘heavy’ indicating ENAs with a mass significantly larger than that of atomic oxygen and a resulting time-of-flight much longer than that of oxygen. Whereas mainly H- and O-group ENAs are released from the surface for incident protons up to 33 keV, the heavier O^+ projectiles also efficiently sputter Na and Cl atoms, water molecules, O_2, H_2O_2 or complexes of several water molecules from the ice block with significant efficiency. All of these are candidates for the observed ‘heavy’ ENA component with very long time-of-flight, but not all of them are equally well detected by JNA: water complexes are very likely sputtered from the ice (Lancaster et al., 1979) but have a rather low probability to remain intact during the interaction with the charge conversion surface in the JNA prototype sensor. H_2O_2 produced by ion irradiation of the target (Loeffler et al., 2006) is also a candidate for the heavy ENA component, but the expected concentrations are small, and again, it is unlikely that this molecule survives the charge conversion surface interaction in the JNA sensor intact. The JNA detection efficiency for chlorine is low due to its large electro-negativity; it would need to form a positive chlorine ion during interaction with the JNA charge conversion surface. It is thus unlikely that the heavy signal is due to the detection of chlorine. The most likely candidate for the measured signal is Na. Sodium is likely ionized on the instrument’s charge conversion surface due to its low ionization energy, and it should thus be easily detected by the JNA prototype. Unfortunately, the detection efficiency of the JNA prototype for energetic neutral Na or Cl or possible water clusters and the shape of the corresponding time-of-flight spectra are not known at present; they will be determined during JNA flight model calibrations. For the analysis shown here, it was assumed that the water molecules and the heavy component have the same detection efficiency as energetic oxygen, and the shape of the time-of-flight spectrum of the ‘heavy’ component was empirically determined.

Signal strength in each of the ENA mass groups was determined by fitting H, O-group and residual ‘heavy’ components to the measured time-of-flight spectra for each energy band separately. The resulting count rates for each mass group were then converted using the JNA geometric factor to differential number flux j in units ($cm^{-2}\ sr^{-1}\ eV^{-1}\ s^{-1}$). To compensate for a varying incident ion beam intensity, this differential flux was then normalized using the incident ion beam flux, which resulted in a normalized ENA flux F in units ($sr^{-1}\ eV^{-1}$):

$$F(E,p,s) = \frac{j(E,s)}{I(p)}$$

where I is the integrated flux of the impinging ion beam in units ($cm^{-2}\ \ s^{-1}$), p is the incident ion species and s is the measured ENA species. The value of F depends on the experiment geometry; the values presented here are specific for the geometry shown in Fig. 1. Fig. 3 shows a summary of the measured energy spectra of the normalized flux for different combinations of primary beam and secondary particle species. For the data shown, the error bar includes the uncertainty of the geometric factor and the uncertainty due to counting statistics. As a general trend, the observed ENA intensities are higher for a larger ratio of projectile mass to emitted ENA mass, e.g., protons are rather inefficient for producing ‘heavy’ ENAs (Fig. 3e), whereas incident oxygen ions produce more than an order of magnitude larger ENA fluxes (Fig. 3f).

4. Discussion

4.1. Energy spectra

The recorded energy spectra can be divided into four types (or a combination of these): (1) spectra where the incoming particles are directly reflected as ENAs (Fig. 3a and d), (2) spectra where recoil particles are generated from the ice surface (collisional sputtering, Fig. 3b), (3) energy spectra where the incident species has too high energy to be directly recorded as reflected ENAs and where products from electronic sputtering dominate in the energy range where measurements are made (Fig. 3, all panels for ion energies ≫3 keV), and (4) H ENA spectra obtained from incident oxygen ions with sufficiently high energy. In this case, the incident ion is heavy enough to produce a significant molecular H_2O ENA flux that likely dissociates at the instruments charge conversion surface, thus creating an artificial H ENA signal (Fig. 3b, for incident ion energies of 18 keV and above). Examples of these four types are discussed in detail below.

Fig. 4 shows an example of the first type of energy spectrum of reflected hydrogen ENAs generated from incident low energy (1 keV) protons, along with a fitted Maxwell distribution, as derived by Futaana et al. (2012). The observed energy spectrum is well reproduced by the fit, which suggests that the particles are scattered from the ice surface similar to particles scattered from the regolith on the lunar surface. For incident 1 keV protons, the characteristic energy of hydrogen backscattered from the lunar regolith is $k_BT = 117$ eV (Futaana et al., 2012). For the ice scattering case $k_BT = 165$ eV was found. This value is somewhat sensitive to the shape of the JNA instrument energy acceptance function. Variations of this function within its confidence limits resulted in characteristic energies ranging from 146 eV to 191 eV for the same data. These characteristic energies are 1.5–2 times higher than the typical case of scattering from the lunar regolith. This may be due to being much closer to the normal angle of incidence in the lunar regolith case shown in Futaana et al. (2012) compared with the grazing angle of 83° used in this study. The obtained reflection fraction from ice of 0.28 for incident protons at 1 keV is, however, almost the same as the hydrogen reflection coefficient of 0.19 reported for the lunar regolith, as measured using an almost identically built instrument on Chandrayaan-1 (Wieser et al., 2009; Futaana et al., 2012; Vorburger et al., 2013).

An example of the second type of energy spectrum is shown in Fig. 5: incident oxygen ions with 3 keV energy create recoil

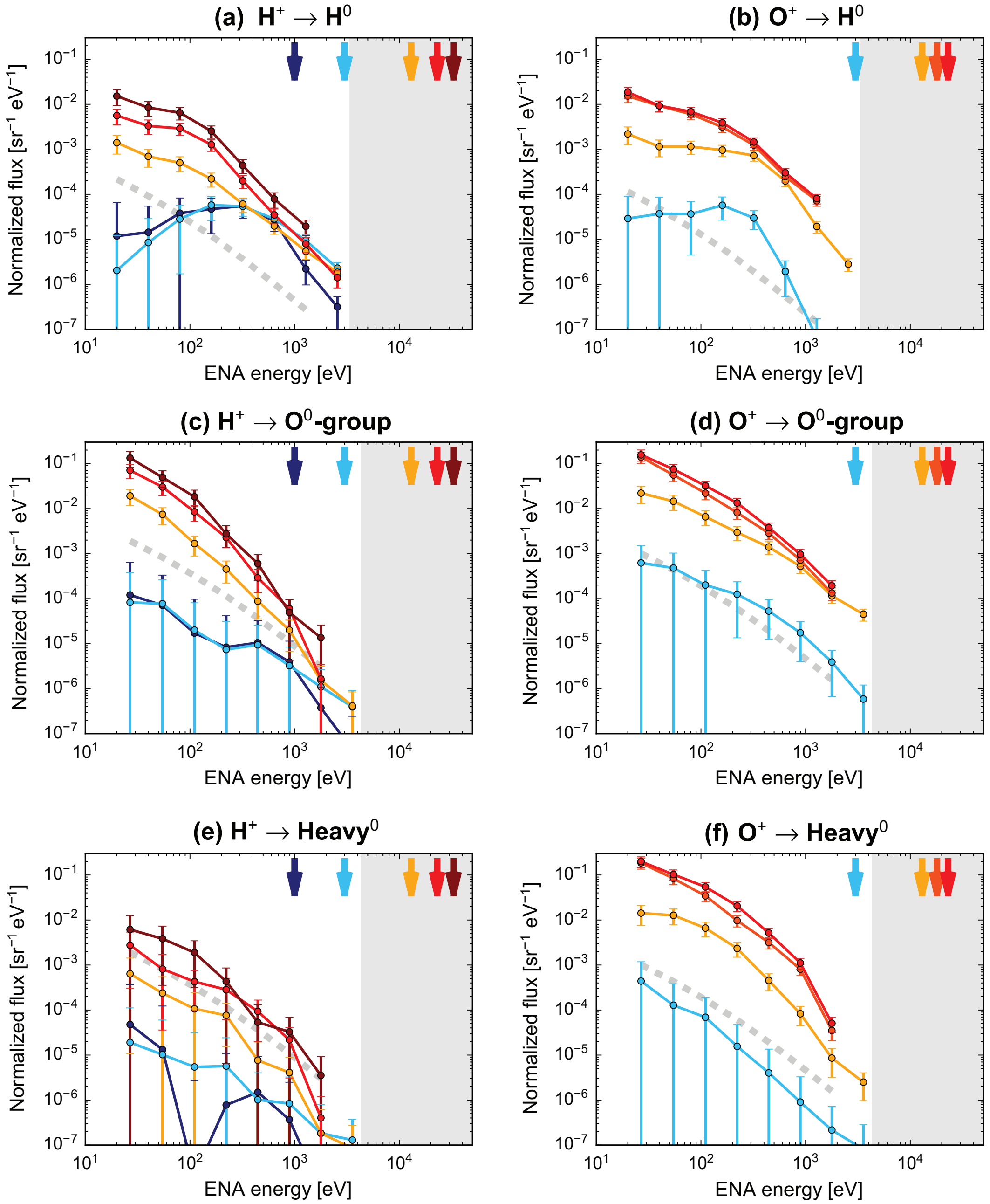

Fig. 3. ENAs spectra measured for incident protons (panels a, c and e) and incident oxygen ions (panels b, d and f) and different emitted ENA mass groups (H, O-group and, Heavy). The energy spectra are normalized with the incident flux onto the ice target. The colored arrows represent the incident ion beam energy, which belongs to an energy spectrum of the same color. The gray dashed line represents an average one-count limit for the measurements shown. The ENA energy range not accessible by the JNA sensor is denoted with a gray background.

hydrogen ENAs. Their upper energy limit is well modeled by a single elastic collision of the O^+ projectile with a hydrogen atom on the surface (Niehus et al., 1993). In general, collisional sputtering dominates at low energies, with total yields that are fairly independent of incident energy (Johnson, 1998). The energy E_R of a target recoil particle from a single elastic collision is given by

$$E_R = E\frac{4A\cos^2\delta}{(1+A)^2}, \quad \text{for } \delta \le 90^\circ$$

with M_1 being the mass of the projectile, M_2 being the mass of the recoil particle and the mass ratio A defined as $A = M_2/M_1$. E denotes the incident ion energy and $\delta = 180°–\theta–\phi$ is the total deflection angle for this experiment (Fig. 1).

An example of the third type of energy spectra is shown in Fig. 6, i.e., the energy spectrum of neutral oxygen produced from an incident 33 keV hydrogen ion beam. Fitting with a Maxwell distribution does not reproduce the shape of the measured spectrum. This indicates that the observed ENAs are not due to a single collision scattering process or collisional sputtering. A reasonable fit for the energy spectrum $F(E)$ is obtained using a Thompson–Sigmund formula that models electronic sputtering (Sigmund, 1969), modified to account for the masses of the projectile and the emitted ENA (Betz and Wien, 1994):

$$F(E) \propto \frac{E}{(E+E_b)^3}\left(1-\sqrt{\frac{E}{E_b+E_i'}}\right)$$

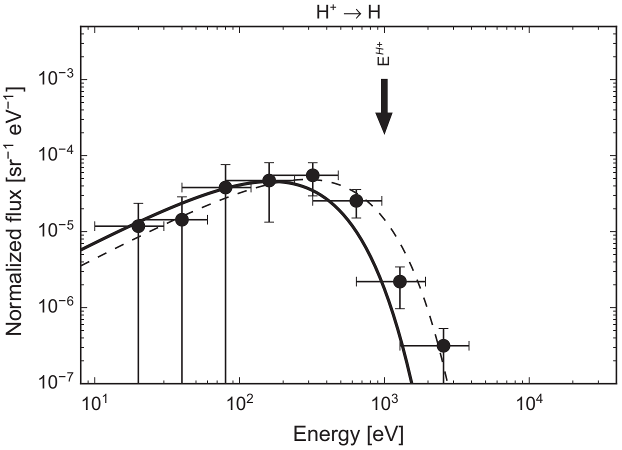

Fig. 4. Measured energy spectra of the hydrogen ENA differential flux from the ice surface, normalized to the incident flux prior to deconvolution of the instrument energy response function (circles) for an incident 1 keV proton beam (arrow). A fit to the measured energy spectra consisting of a Maxwell distribution convoluted with the instrument energy response is shown as a dashed line. The Maxwell component only is shown as a solid line and has a characteristic energy of $k_BT = 165$ eV. Error bars on the *x*-axis indicate the energy bin width of the instrument; error bars on the *y*-axis represent measurement uncertainties.

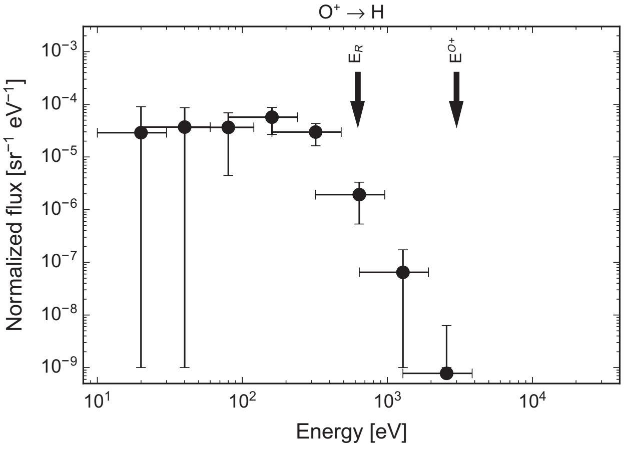

Fig. 5. The energy spectrum of the hydrogen ENA differential flux from the ice (circles) for incident O⁺ ions with $E^{O+} = 3$ keV (right arrow). An upper energy limit for the recoil energy is at $E_R = 625$ eV (left arrow). Error bars have the same meaning as in Fig. 4.

$$E_i' = 4E_i\frac{M_1M_2}{(M_1+M_2)^2}$$

where E is the energy of the emitted ENA, E_b is the surface binding energy of 2–4 eV (Wurz and Lammer, 2003), and M_1 and M_2 are the mass of the projectile and the emitted ENA, respectively. The spectrum has a characteristic cut-off energy of $E_{co} = E_i' - E_b$, which, for this example, is above the energy range covered by the experiment.

A fourth type of observed energy spectra is related to H ENA spectra only; Fig. 7 shows such a H ENA spectrum, along with the corresponding O-group ENA spectrum, both of which are produced from the same incident 23 keV oxygen ion beam. The H ENA component is well modeled by assuming that the O-group signal consists entirely of energetic H_2O molecules and that some of these molecules dissociate at the instruments charge conversion surface, thus creating an artificial H ENA signal. Energy dependent dissociation fractions for incident H_2O ENAs at the JNA charge conversion surface are, unfortunately, not yet known. A simple model for this artificial H ENA signal reproduces at least the low-energy part of the H ENA spectrum. In this model, complete dissociation for 1280 eV H_2O molecules at the charge conversion surface and an energy proportional dissociation fraction (van Slooten et al., 1991) below 1280 eV are assumed. Because the dissociation occurs prior to energy analysis, the hydrogen fragments appear downshifted in the energy spectrum, with an energy $E_H = E_{H2O}/m_{H2O} * m_H$ if no energy losses on the charge conversion surface are considered (Fig. 7, H-model). This model can explain all of the H ENA flux below 100 eV. However, the same model applied to lower energy incident oxygen ions ($E < 18$ keV) predicts more than an order of magnitude larger H ENA fluxes than were observed. Thus, in these cases, the O-group ENAs likely consist mostly of atomic oxygen and not water molecules.

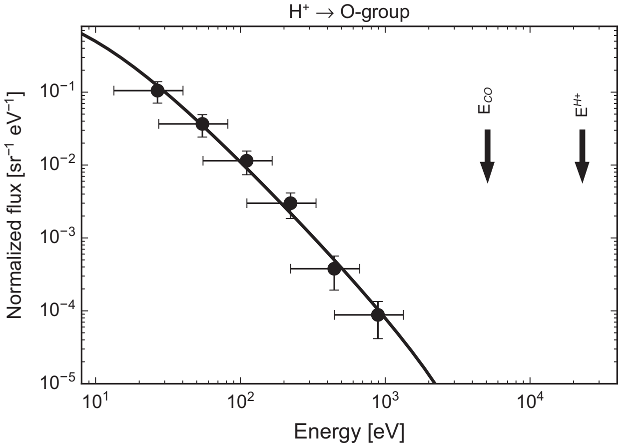

Fig. 6. Energy spectrum of oxygen group ENAs sputtered by the 33 keV proton beam (circles). The right arrow indicates the energy of the impinging ions. A fit using the Thompson–Sigmund spectra (solid line) and its cutoff energy E_{co} of 5100 eV (left arrow) are also shown. Error bars have the same meaning as in Fig. 5.

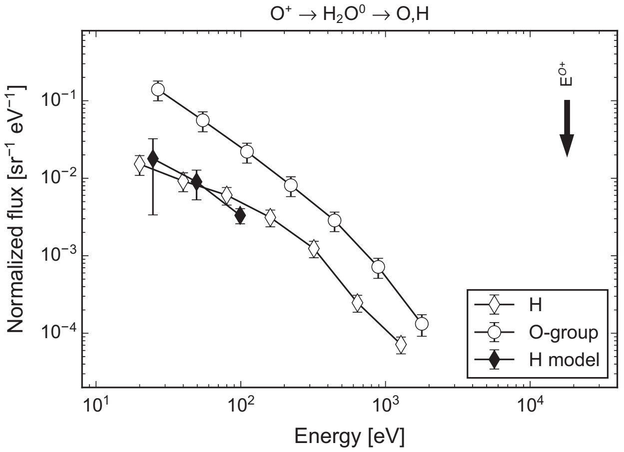

Fig. 7. Energy spectrum of oxygen-group ENAs sputtered by the 23 keV oxygen ion beam (open circles) and the corresponding H ENA signal (open diamonds). The H-ENA signal is compatible with all of the oxygen-group ENA signal being produced by energetic H_2O dissociating at the JNA charge conversion surface, at least for energies above 200 eV. The modeled H ENA background, originating from the dissociation of energetic neutral H_2O, is shown with filled diamonds.

4.2. ENA yield

From Fig. 3, the energetic neutral particle yield Y_{ENA}, which is the ratio between the total number of emitted energetic neutral particles above an energy threshold E_{min} and the total number of incident ions, is calculated as the angular integral of the normalized ENA flux, F. Assuming a non-isotropic angular distribution of the emitted particles proportional to $\cos^{4/3}\theta$, where θ is the angle to the surface normal (Vidal et al., 2005), the integral ENA yields Y_m for the three mass groups $m = \mathrm{H}$, O-group or 'Heavy' in the energy range covered by JNA are estimated by using

$$Y_m = k \int_{E_{\min}}^{E_{\max}} F_m(E)\, dE$$

$$Y_{\mathrm{ENA}} = Y_{\mathrm{H}} + Y_{\text{O-group}} + Y_{\mathrm{Heavy}}$$

with $E_{\min} = 15$ eV and $E_{\max} = 3.3$ keV. The factor k ensures proper normalization to the assumed $\cos^{4/3}\theta$ angular distribution of the emitted ENA flux and the actual observation direction of 83° to the surface normal. A summary of yields is shown in Fig. 8. When adding the yields for the different mass groups, the total energetic neutral particle yield Y_{ENA} is obtained. An empirical model of sputtering yields from pure water ice surfaces is described by Famá et al. (2008) and shown for comparison. Data for this model were mostly derived from relatively flat thin ice films (e.g., Baragiola et al., 2003). Sputter yields for rough surfaces are similar to the sputter yields of flat surfaces at smaller incidence angles (Küstner et al., 1998). This is because for a rough surface and a given fixed macroscopic incidence angle, on the microscopic level, which is seen by the impinging particles, a broad range of incidence angles occur at the same time. Furthermore, on a rough surface, the sputtering yield is lower than that of a flat surface due to the re-deposition of sputtered products (Küstner et al., 1999; Loeffler et al., 2009). We estimate that the sputtering yields at an 83° macroscopic angle of incidence, as used in our setup, correspond approximately to the sputtering yields from a flat surface at an ~60° angle of incidence (Küstner et al., 1999). Including this correction for the incident angle, our measurements are compatible with the model of Famá et al. (2008), as discussed below, despite the ice temperature of 150 K being outside the parameter range this model was made for ($T < 140$ K). The model expresses the total sputtering yield Y as

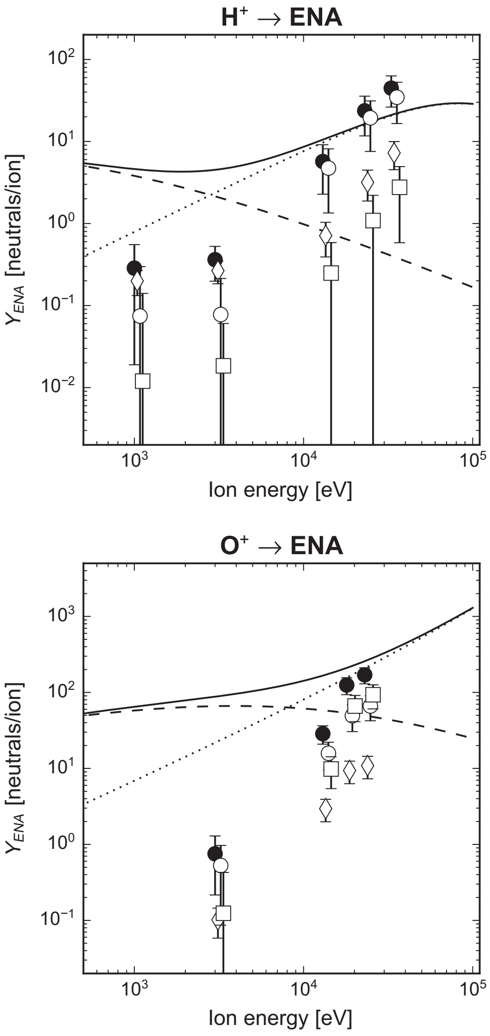

Fig. 8. Energetic neutral particle yields, Y_{ENA}, for incident protons (top panel) and oxygen ions (bottom panel). Different symbols represent mass groups of emitted neutrals: H (open diamonds), O-group (open circles), Heavy-group (open squares), and their sum (filled circles). The data points for the oxygen-group and the 'heavy' ENAs are slightly shifted to the right on the energy axis for easier reading. For incident oxygen ions of 18 keV and 23 keV, the O-group likely consists of H_2O molecules and the corresponding H ENA signal may result from their dissociation in the JNA instrument. The expected total molecular sputtering yield Y, modeled after Famá et al. (2008) for an angle of incidence of 60° (see text), is shown as a solid line for comparison, along with its collisional component Y_n (dashed line) and electronic component Y_e (dotted line).

$$Y \approx Y_n + Y_e$$

with Y_n being the contribution from collisional sputtering proportional to the nuclear-stopping cross section and Y_e, the contribution from electronic sputtering proportional to the square of the electronic stopping cross section. The former dominates at lower energies, and the latter does so at higher energies. The two components are reflected in the energy spectra of the emitted energetic neutrals, with collisional processes generating more peaked energy spectra (e.g., Fig. 4) and electronic sputtering generating an E^{-2} dependence (e.g., Fig. 6). In the collisional domain, it is likely that the emitted energetic neutrals originate from the incident primary ion, whereas in the electronic domain, the emitted energetic neutrals originate from the ice itself. This results in $Y_{\mathrm{ENA}} \approx Y_{\mathrm{H}}$ for incident protons at lower energies and $Y_{\mathrm{ENA}} \approx Y_{\mathrm{O}}$ at higher incident energies (Fig. 8, top panel). Y_{ENA} is always smaller than the total sputtering yield because Y_{ENA} only includes the energetic neutral particle fraction emitted from the surface with energies above $E_{\min}$. The relative difference between Y_{ENA} and the total sputtering yield is larger for impinging ion energies below a few keV because fewer energetic neutrals with energies above $E_{\min}$ are generated (Wurz and Lammer, 2003; Wurz et al., 2007). Additionally, at low impinging ion energy, the obtained Y_{ENA} is more uncertain due to the assumption of the energetic neutral flux being emitted according to a $\cos^{4/3}\theta$ angular distribution; e.g., for protons impinging on lunar regolith, a tri-modal angular energetic neutral atom flux distribution with an enhancement in both the specular reflection and impinging direction is observed (Schaufelberger et al., 2011). In our data, Y_{ENA} exceeds the model predicted total sputtering yield slightly for impinging hydrogen ions above 20 keV, which reflects the uncertainty in the scaling of the model to our application. Impurities in our ice sample (CO_2, hydrohalite, air) may also affect the observed energetic neutral particle yield. Impurities can increase the sputtering yield via the formation of more volatile species. The most volatile species in the surface are sputtered most efficiently; however, after sufficient exposure to the impinging ions, the composition of the sputtered material approaches bulk composition (Johnson, 1998). The concentration of impurities in our water ice was a few percent, with the dominant impurity component being the hydrohalite. Although this concentration may affect the observed sputtering yield, a comparative measurement in the same setup with pure water ice or pure hydrohalite would be needed to quantify it.

5. Conclusions

We measured energy spectra of sputtered energetic particles from salty water ice under Ganymede-like conditions under ion bombardment. The energy spectrum of the neutral atom flux emitted from the ice could, in some cases, be fitted with Maxwellian distributions, which is indicative of particle reflection on the surface. For higher incident energies, where electronic sputtering becomes dominant, the energy spectrum changed to a Sigmund–Thompson shape. A very high hydrogen ENA yield of 0.20 for 1 keV incident protons was observed. Hydrogen ENA yields of $\sim$7 were measured for 33 keV incident protons. Oxygen and other heavier ENAs produced by incident protons generally exhibited a Sigmund–Thompson spectrum, although the intensities were rather low due to mass mismatch between the incident and sputtered particles. The total energetic neutral particle yield for incident protons, with all measured ENA species combined, ranged from 0.28 at 1 keV to $\sim$40 at 33 keV incident ion energy.

Incident oxygen ions, which favored electronic sputtering in the energy range used, resulted in a yield for oxygen or water ENAs up to $\sim$100 for 23 keV incident ion energy. For oxygen ions with an incident energy of 3 keV, the observed oxygen ENA yield was 0.5. Additionally, at the same incident energy, a recoil process was observed, producing a distinct hydrogen ENA signal with a yield of 0.10. Total energetic neutral particle yield for incident oxygen ions ranged from 0.8 at 3 keV to $\sim$170 at 23 keV incident ion energy.

Acknowledgment

P.W. thanks the Swiss National Science Foundation for their financial support.

References

Barabash, S., et al., 2009. Investigation of the solar wind–Moon interaction onboard Chandrayaan-1 mission with the SARA experiment. Curr. Sci. 96 (4), 526–532.

Barabash, S. et al., 2013. Particle environment package (PEP). European Planetary Science Congress 2013, held 8–13 September in London, UK. <http://meetings.copernicus.org/epsc2013> ID EPSC2013-709, 8:709.

Baragiola, R.A., et al., 2003. Sputtering of water ice. Nucl. Instrum. Methods Phys. Res. Sect. B 209, 294–303. doi:10.1016/S0168-583X(02)02052-9, <http://www.sciencedirect.com/science/article/pii/S0168583X02020529>.

Betz, G., Wien, K., 1994. Energy and angular distributions of sputtered particles. Int. J. Mass Spectrom. Ion Process. 141, 1–110.

Cooper, J.F., et al., 2001. Energetic ion and electron irradiation of the icy Galilean satellites. Icarus 149 (1), 133–159. doi:10.1006/icar.2000.6498.

Famá, M., Shi, J., Baragiola, R.A., 2008. Sputtering of ice by low-energy ions. Surf. Sci. 602 (1), 156–161 <http://www.sciencedirect.com/science/article/pii/S0039602807009879>.

Futaana, Y., et al., 2012. Empirical energy spectra of neutralized solar wind protons from the lunar regolith. J. Geophys. Res. 117 (E5). doi:10.1029/2011JE004019.

Futaana, Y., et al., 2015. Low-energy energetic neutral atom imaging of Io plasma and neutral tori. Planet. Space Sci. 108, 41–53. doi:10.1016/j.pss.2014.12.022.

Grasset, O., et al., 2013. JUpiter ICy moons Explorer (JUICE): An ESA mission to orbit Ganymede and to characterise the Jupiter system. Planet. Space Sci. 78, 1–21. doi:10.1016/j.pss.2012.12.002.

Ip, W.-H., et al., 1997. Energetic ion sputtering effects at Ganymede. Geophys. Res. Lett. 24 (21), 2631–2634. doi:10.1029/97GL02814.

James, P.B., Kieffer, H.H., Paige, D.A., 1992. The seasonal cycle of carbon dioxide on Mars. In: , Mars. University of Arizona Press, Tucson, pp. 934–968.

Johnson, R.E., 1998. Sputtering and desorption from icy surfaces. In: , Solar System Ices, vol. 227. Astrophysics and Space Science Library, p. 303.

Kazama, Y., et al., 2007. Development of an LENA instrument for planetary missions by numerical simulations. Planet. Space Sci. 55, 1518–1529.

Khurana, K.K., 1997. Euler potential models of Jupiter's magnetospheric field. J. Geophys. Res.: Space Phys. 102 (A6), 11295–11306. doi:10.1029/97JA00563, ISSN: 2156-2202.

Khurana, K.K., et al., 2007. The origin of Ganymede's polar caps. Icarus 191 (1), 193–202.

Küstner, M., et al., 1998. The influence of surface roughness on the angular dependence of the sputter yield. Nucl. Instrum. Methods B 145, 320–331.

Küstner, M., et al., 1999. Angular dependence of the sputtering yield of rough beryllium surfaces. J. Nucl. Mater. 265 (1–2), 22–27. doi:10.1016/S0022-3115(98)00648-5.

Lancaster, G.M., et al., 1979. Secondary ion mass spectrometry of molecular solids: Cluster formation during ion bombardment of frozen water, benzene, and cyclohexane. J. Am. Chem. Soc. 101, 1951–1958.

Loeffler, M.J., et al., 2006. Synthesis of hydrogen peroxide in water ice by ion irradiation. Icarus 180 (530), 265–273.

Loeffler, M.J., Dukes, C.A., Baragiola, R.A., 2009. Irradiation of olivine by 4 keV He^+: Simulation of space weathering by the solar wind. J. Geophys. Res. 114, E03003. doi:10.1029/2008JE003249.

McCarthy, C., et al., 2007. Solidification and microstructures of binary ice-i/hydrate eutectic aggregates. Am. Mineral. 92 (10), 1550–1560.

McCord, T.B., et al., 1998. Non-water-ice constituents in the surface material of the icy Galilean satellites from the Galileo near-infrared mapping spectrometer investigation. J. Geophys. Res.: Planets 103 (E4), 8603–8626. doi:10.1029/98JE00788.

McCord, T.B., et al., 1997. Organics and other molecules in the surface of the icy Galilean satellites. Science 278, 271–275.

Marti, A., et al., 2001. New calibration facility for solar wind plasma instrumentation. Rev. Sci. Instrum. 72 (2), 1354–1360.

Murphy, D.M., Koop, T., 2005. Review of the vapour pressures of ice and supercooled water for atmospheric applications. Quart. J. Roy. Meteorol. Soc. 131 (608), 1539–1565.

Niehus, H., Heiland, W., Taglauer, E., 1993. Low-energy ion scattering at surfaces. Surf. Sci. Rep. 17, 213–303.

Schaufelberger, A., et al., 2011. Geophys. Res. Lett. 38, L22202. doi:10.1029/2011GL049362.

Shi, M., et al., 1995. Sputtering of water ice surfaces and the production of extended neutral atmospheres. J. Geophys. Res.: Planets 100 (E12), 26387–26395. doi:10.1029/95JE03099.

Showman, A.P., Malhotra, R., 1999. The Galilean satellites. Science 286 (5437), 77–84.

Sigmund, P., 1969. Theory of sputtering. I. Sputtering yield of amorphous and polycrystalline targets. Phys. Rev. 184, 383–416.

van Slooten, U., et al., 1991. Scaling law for dissociation of fast molecular hydrogen scattered from Ag (1 1 1). Chem. Phys. Lett. 185 (5–6), 440–444.

Vidal, R.A., et al., 2005. Angular dependence of the sputtering yield of water ice by 100 kev proton bombardment. Surf. Sci. 288, 1–5.

Vorburger, A., et al., 2013. Energetic neutral atom imaging of the lunar surface. J. Geophys. Res.: Space Phys. 118, 3937–3945. doi:10.1002/jgra.50337.

Wieser, M., Wurz, P., 2005. Production of a 10 eV–1000 eV neutral particle beam using surface neutralization. Meas. Sci. Technol. 16, 2511–2516.

Wieser, M., et al., 2009. Extremely high reflection of solar wind protons as neutral hydrogen atoms from regolith in space. Planet. Space Sci. 57 (14–15), 2132–2134. doi:10.1016/j.pss.2009.09.012.

Wieser, M., et al., 2010. First observation of a mini-magnetosphere above a lunar magnetic anomaly using energetic neutral atoms. Geophys. Res. Lett. 37 (5). doi:10.1029/2009GL041721.

Wurz, P., Lammer, H., 2003. Monte-Carlo simulation of Mercury's exosphere. Icarus 164 (1), 1–13.

Wurz, P., et al., 2007. The lunar exosphere: The sputtering contribution. Icarus 191, 486–496. doi:10.1016/j.icarus.2007.04.034.

Wurz, P., et al., 2010. Self-consistent modelling of Mercury's exosphere by sputtering, micro-meteorite impact and photon-stimulated desorption. Planet. Space Sci. 58, 1599–1616.